



## PLATE IMPACT EXPERIMENTS FOR INVESTIGATING INELASTIC DEFORMATION AND DAMAGE OF ADVANCED MATERIALS

H. D. Espinosa and R. J. Clifton  
Division of Engineering  
Brown University  
Providence, Rhode Island

### ABSTRACT

Several types of plate impact experiments are discussed from the perspective of their usefulness in studying the dynamic inelastic response of such advanced materials as ceramic/metal composites. These experiments are illustrated by their application to an AlN/AlN/Al composite developed by Lanxide Armor Products, Inc. Pressure-shear waves are used to determine the shearing resistance of the material at high shearing rates. Soft-recovery, normal impact experiments using an eight-pointed star-shaped flyer are used, along with TEM and SEM, to investigate the principal mechanisms of failure under known stress histories. Extensions of the pressure-shear technique to applications involving hard specimens are presented. One interesting extension is the development of the capability for monitoring the normal and in-plane components of the motion at the interface between the rear surface of the specimen and the transparent window plate. This capability makes it possible to monitor the shearing resistance before unloading waves can interfere with the results by causing tensile damage to the specimen or a back-up plate.

### 1. INTRODUCTION

New challenges in material characterization are encountered with the development of modern high performance ceramics and composites. Tailor-made composites that optimize materials performance for a wide variety of applications are currently manufactured. Their hardness, chemical inertness, low density, high temperature capability and wear resistance make these materials attractive possibilities for many advanced technologies.

Plate impact experiments offer unique capabilities for their characterization under different loading conditions. These experiments allow high stresses, high pressures, high strain rates and finite deformations to be generated under well characterized conditions. The testing techniques can be divided into two categories: a) stress wave propagation tests (pressure-shear symmetric impact and soft-recovery normal impact) and b) nominally homogeneous deformation tests (pressure-shear sandwich configuration). They all rely on the generation of one dimensional waves in the central region of the specimen in order to allow a clear interpretation of the experimental results and the mathematical modelling of the material behavior. In the soft-recovery normal impact experiment, see Fig. 1a, an eight pointed star-shaped flyer impacts a square sample, subjecting the central octagonal region to a plane pulse. A tensile pulse is originated from a gap between the specimen and the momentum trap upon reflection of the compressive pulse. The velocity-time profiles recorded at the rear surface of the momentum trap plate enable the evaluation of models of inelastic response in compression and tension. In addition, the specimens are recovered intact, allowing their study by means of electron microscopy. This study provides the basis for the identification of the phases and micromechanical processes that control the damage and plastic response of the material. In the second category, a thin plate specimen, Fig. 2a, is sandwiched between two elastic plates subjecting the material to shear strain rates greater than  $1 \times 10^5 \text{ sec}^{-1}$ . The inelastic response is obtained by monitoring the wave profile at the rear surface of the anvil plate. In the case of symmetric pressure-shear impact, in the first category, a flyer plate impacts the specimen plate at a skewed angle. The combined

longitudinal and transverse waves generated by impact, impose different stress histories at each section of the specimen (see Fig. 3). These stress-time histories are also functions of the stress-induced damage which affects the velocity-time profiles that are recorded during the experiments. These data are used to assess the validity of the numerical modelling of the material behavior.

The pressure-shear impact configuration requires some modifications for the study of hard materials with low fracture toughness. To this end, a new window interferometer has been developed for pressure-shear experiments to extend their capabilities to such materials. The advantages and applications that are derived from the technique are discussed in detail.

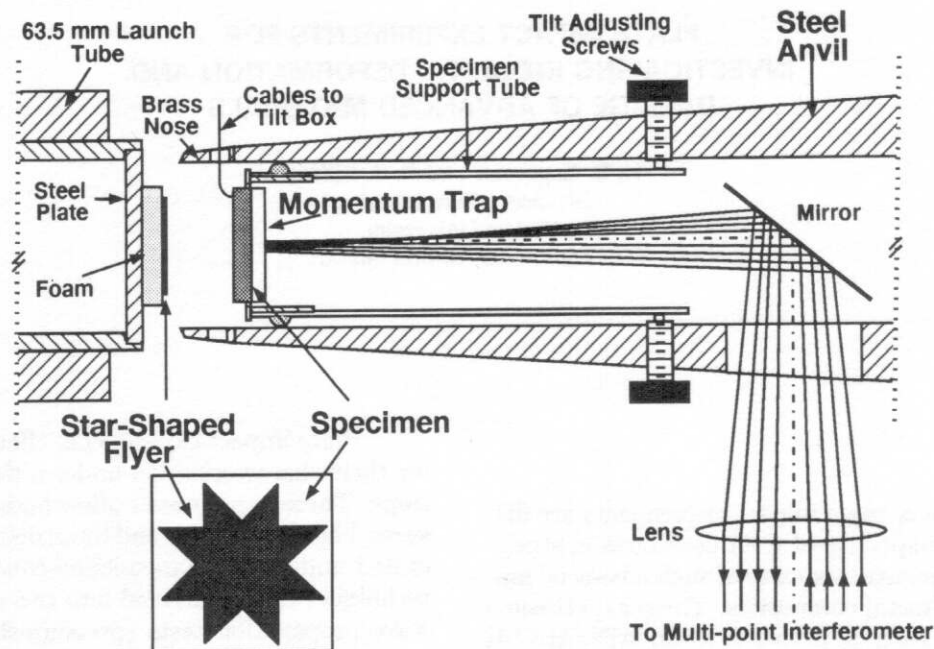


Figure 1a: Soft recovery normal impact configuration.

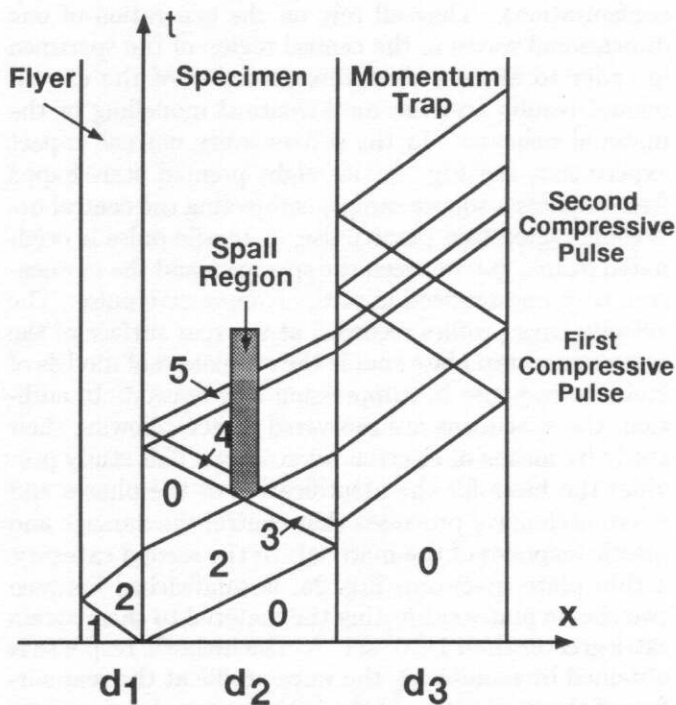


Figure 1b: Lagrangian t-X diagram for soft recovery experiment.

## 2. THE MATERIAL

Although the methodology presented here is intended to be applicable to a wide range of materials, the results reported are for one material: an aluminum nitride-aluminum matrix reinforced by aluminum nitride particles (AlN/AlN/Al), which has been developed by Lanxide Armor Products, Inc. Specifically, this composite material consists of aluminum nitride (AlN) reinforcement particles with a mean diameter of  $3 \mu\text{m}$  and a matrix of AlN/Al, with AlN referred to as the reaction product. The material is manufactured using the DIMOX<sup>TM</sup>, directed metal oxidation process. The process starts with the formation of a porous preform of reinforcement particles held together with an added binder. The AlN/Al matrix growth involves the reaction of a molten aluminum alloy, Al-Sr-Si-Ni, in a nitrogen atmosphere. Under certain conditions of temperature and nitrogen pressure the AlN reaction product grows outward from the original alloy surface. Molten aluminum alloys are drawn continuously, along microscopic channels through its own nitridation product, thereby sustaining the growth process. Fig. 4 is a SEM backscattering electron micrograph that shows the microstructure of the ceramic-reinforced composite. AlN particles

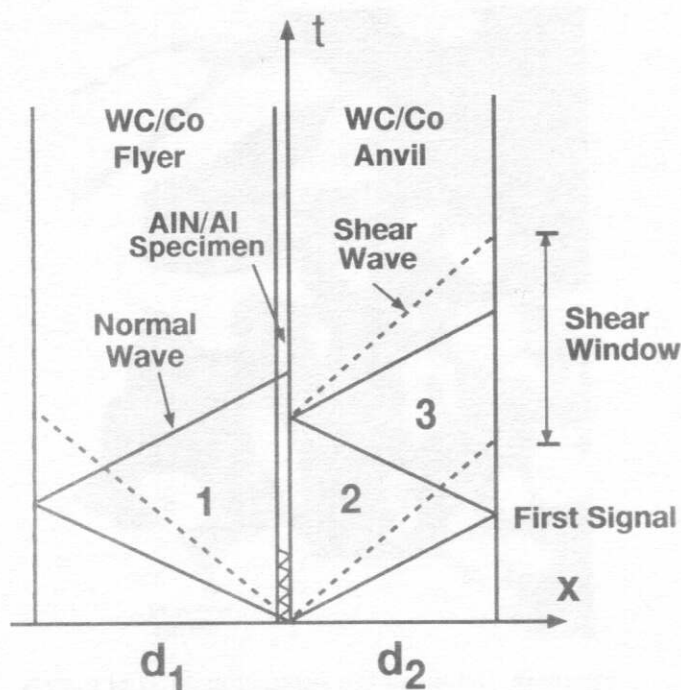


Figure 2a: Lagrangian t-X diagram for high strain rate pressure-shear experiment.

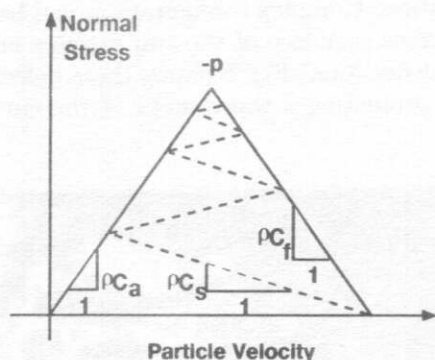


Figure 2b: Loci of states of normal stress and particle velocity for flyer, anvil and specimen.

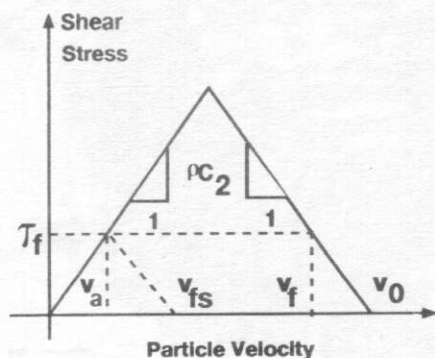


Figure 2c: Loci of states of shear stress and transverse particle velocity for flyer, anvil and specimen.

with size ranging from submicron to 20  $\mu\text{m}$  can be observed. An interconnected AlN reaction product with some interconnected metal phase results in an AlN/Al matrix. The metallic phase is present as both interconnected tortuous channels and pockets. A TEM picture showing the AlN filler and the submicron AlN reaction product grains in the AlN/Al matrix is given in Fig. 5. The micrograph shows that the material has no appreciable porosity. The AlN/Al matrix, Moiré fringes can be observed at the overlapping region between grains. This feature reveals that the formed AlN reaction product has a grain size of the order of 100 nm, see Fig. 6. The addition of transition metals in the aluminum alloy is believed to contribute to the high refinement of the microstructure, A. Nagelberg, 1989; D. Creber et al., 1988. By changing the beam direction with respect to the thin foil, a *spine-like* microstructure is observed (see Fig. 7).

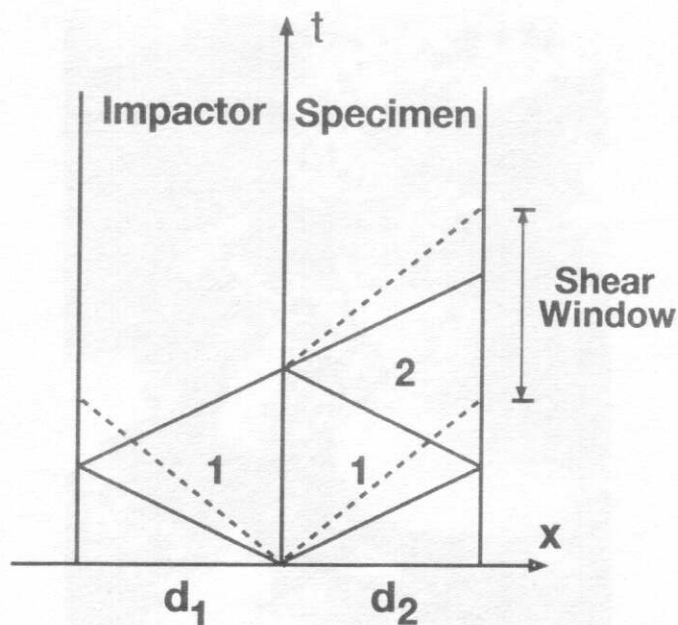
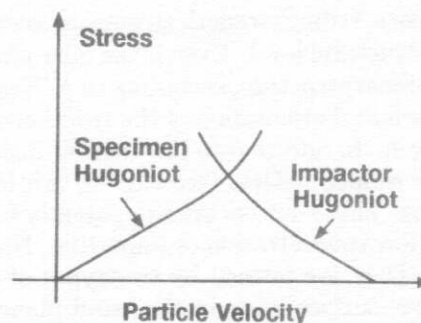


Figure 3: Lagrangian t-X diagram for symmetric pressure-shear experiment.



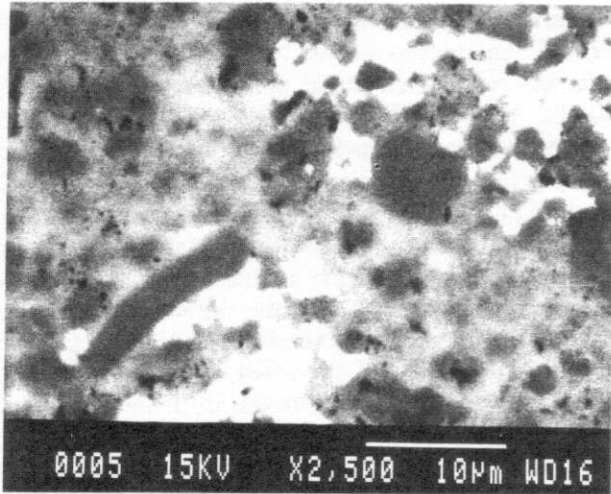


Figure 4: SEM backscattering electron micrograph showing the different interconnected phases present in the microstructure.

As a consequence, strong strength anisotropy is expected at this microstructural level. Even if the filler phase disrupts the columnar structure, according to A. Nagelberg, 1989, some preferred orientation of the reaction product seems to remain. In addition to low density dislocation defects, dome shaped defects (see Fig. 8) are found in the AlN grains. These defects arise apparently from the presence of a low concentration of impurities, Hagege S. et al., 1988. They are formed by two types of faulted surfaces, (a flat surface lying in the basal plane of the wurtzite structure and a curved surface), connected by



Figure 5: TEM bright field image showing the AlN filler particles and the AlN/Al matrix.



Figure 6: Details of the submicron AlN/Al matrix presenting Moiré fringes at the overlapping regions between grains.

a dislocation. Complex configurations can be formed by a continuous sequence of the two surfaces and the connecting dislocation. Fig. 8 shows these defects with one of them presenting a wavy shape of the curved faulted surface.



Figure 7: Spine-like microstructure of the submicron AlN reaction product and Al alloy phase.



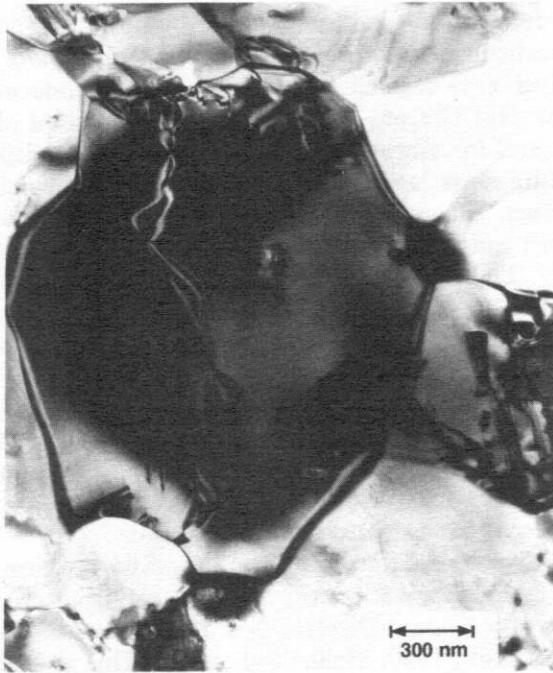


Figure 8: Dome-like defects within the AlN filler particles.

### 3. NORMAL IMPACT SOFT-RECOVERY TESTS

Recovery experiments (Kumar and Clifton, 1979; Clifton et al., 1989; Raiser et al., 1990) offer attractive possibilities for identifying the principal mechanisms of inelasticity in tension and compression. The samples are recovered intact, allowing their study by means of electron microscopy. This feature, together with the real-time stress histories, is used to assess the validity of the constitutive models, (Espinosa et al. 1991a and b). The main objective of this experiment is to provide information on the elastic precursor decay, spall strength and material softening due to microcracking. This experimental configuration focuses on the determination of the onset of such events, rather than the characterization of advanced states of damage and/or plastic deformation.

The configuration is shown in Fig. 1. The projectile is made of a fiberglass tube. At the front, the projectile plate and star-shaped flyer plate are separated by a stiff, low impedance foam. This configuration prevents re-loading of the specimen by reflected waves if the impedance of the flyer is lower than that of the specimen. A Ti-6Al-4V flyer was chosen to have a sufficiently high yield strength for it to remain elastic at the impact veloc-

Material	Density	Longitudinal Wave Speed	Transverse Wave Speed	Acoustic Impedance	Shear Impedance
-	[Kg/cm <sup>3</sup> ]	[mm/μsec]	[mm/μsec]	[GPamm/μsec]	[GPamm/μsec]
Hampden Steel	7861	5.983	3.264	47.03	25.66
Ti-6Al-4V	4430	6.255	3.151	27.71	13.96
AlN/AlN/Al	3165	9.50	5.5	30.07	17.41
WC-6Co	14600	6.70	4.1	97.82	59.86
Sapphire	4000	11.30	6.54	45.2	26.16

Table I : Material Properties

Shot No.	Projectile Velocity	Skew Angle	Specimen Thickness
-	$V_0$ , [mm/μsec]	$\alpha$ , [degrees]	$h$ , [mm]
91-01	.0804	0	3.683
91-02	.1070	0	3.803
91-03	.232	18	4.410
91-04	.231	18	4.028
91-05	.1507	26.6	0.294
91-06	.2129	15	0.260

Shot No.	Normal Stress	Shear Stress	Strain Rate	Experimental Configuration*
-	$\sigma_{11}$ , [GPa]	$\tau$ , [MPa]	$\dot{\gamma}$ , [1/sec]	-
91-01	1.417	475	-	NISR
91-02	1.889	633	-	NISR
91-03	3.317	480	-	PSS
91-04	4.029	754	-	PSSW
91-05	6.590	778	$1.4 \times 10^5$	HSRPS
91-06	10.060	875	$.98 \times 10^5$	HSRPC

\* NISR: Normal Impact Soft-Recovery; † PSS: Pressure-Shear, Symmetric

\* PSSW: Pressure-Shear, Symmetric with Window; HSRPS: High Strain Rate Pressure-Shear

\* HSRPC: High Strain Rate Pressure Change

Table II : Summary of Experimental Results

ities used. At the rear, there is a piston with a keyway, to prevent rotation of the projectile. The target assembly consists of an inner cylinder for supporting the specimen and an outer anvil for stopping the projectile. The anvil has a disposable brass nose which absorbs part of the impact energy. The specimen consists of a square, thin plate of AlN/AlN/Al composite backed up by a plate which, ideally, has matching impedance. This plate flies off the back of the specimen after the main compressive pulse reflects from the rear surface and returns to the interface. For the experiments reported here, the momentum trap was made of Hampden steel, which has a higher impedance than AlN/AlN/Al (See Table II); consequently, a reflected compressive wave is generated at the specimen-momentum trap interface.

### 3.1 General experimental procedure

The plate impact experiments were performed in the 2.5 inch gas gun at Brown. The specimens and momentum traps are squares, 22 mm x 22 mm, with thicknesses reported in table II. In order to ensure that plane waves are generated at impact, all the plates are lapped flat using a 12-inch lapping machine and 14.5  $\mu\text{m}$  alumina powder. After the plates are polished using 0.3  $\mu\text{m}$  alumina, they are placed under an optical flat surface. By illuminating the surface with a monochromatic light source ( $\lambda=587.6\text{ nm}$ ) the flatness of the plates is measured and considered satisfactory if only one interference ring is observed.

In order to generate waves propagating essentially perpendicular to the impact face, the target plate and the flyer were aligned using a technique introduced by Kumar and Clifton, 1977a. For the purpose of alignment and for triggering the oscilloscopes, a multilayer thin film mask is sputtered onto the impact face of the specimen. Since the AlN/AlN/Al composite is conductive, a 1  $\mu\text{m}$  thick insulating layer of  $\text{Al}_2\text{O}_3$  is first sputtered. Then, by using a mask, a 1000 Å thick layer of aluminum is sputtered in the form of four diagonal strip pins at the corners and two ground strips crossing at the center. Through a logical circuit, contact of the four pins gives four voltage steps in the ratio of 1:2:4:8, thereby providing a measurement of the tilt at impact.

The velocity of the projectile is measured just before impact by recording the times of contact of five wire pins placed in the path of the projectile.

The normal motion at four points on the rear surface of the momentum trap plate were monitored by means of a Normal Displacement Interferometer (NDI), Clifton et al., 1990; Mello et al., 1991. This multipoint interferometer allows the identification of non-planar motions that can be correlated with the microcracking process and the unloading waves from the star-shaped flyer. The NDI is a standard Michelson interferometer in which the rear surface of the momentum trap is the moving mirror and one peak-to-peak variation in the light intensity corresponds to a normal displacement of  $\lambda/2$ . A schematic of the optical measurement system is shown in Fig. 9.

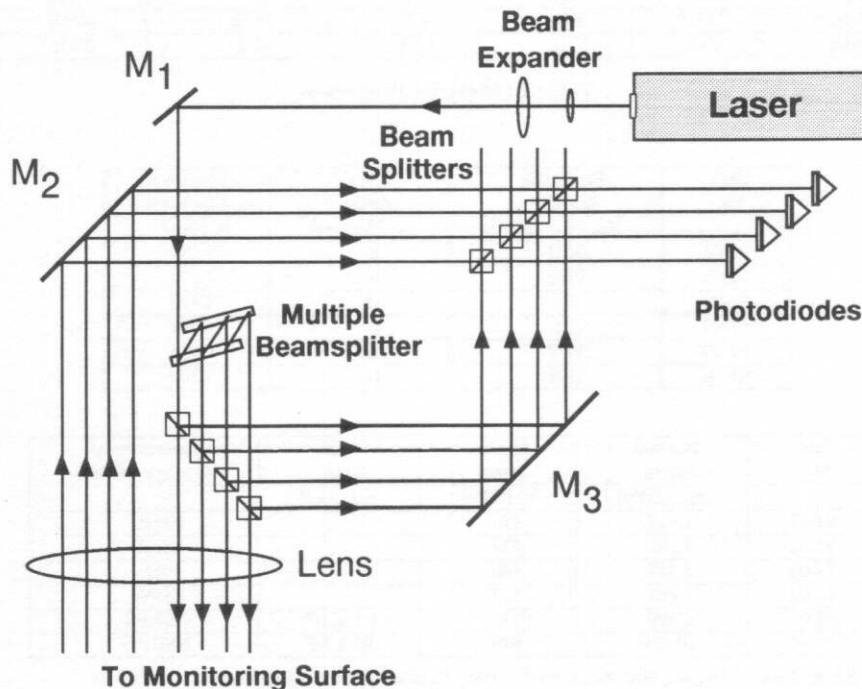


Figure 9: Optical layout of multi-point interferometer.

Thin plates  $5 \times 4 \text{ mm}^2$  were cut from the center of the octagonal region using a low-speed diamond saw. Transmission electron microscopy (TEM) samples were obtained from disks, 3 mm in diameter, cut from these slices using an ultrasonic drill. Both surfaces were ground and polished with diamond polishing wheels, with a final polish using a  $1 \mu\text{m}$  diamond paste. One of the flat surfaces was dimpled by abrasive polishing until a thickness of  $15 \mu\text{m}$  was measured in the central region. Afterwards, the dimple was deepened by ion-milling with argon ions operating at 1 mA, 5 kV and  $15^\circ$  incidence angle, until perforation. The samples were examined using a Phillips EM320 microscope operating at 120 kV. Scanning electron microscopy (SEM) samples were prepared from the thin  $5 \times 4 \text{ mm}^2$  plates by polishing with  $0.5 \mu\text{m}$  alumina and washing with methanol. The operating conditions in the JEOL JSM-840F microscope are given in each micrograph.

### 3.2 Wave propagation analysis

The elastic wave fronts for a plane wave analysis are given in the time-distance (t-X) Lagrangian diagram in Fig. 1b. An elastic analysis provides a starting point for understanding the possible inelastic response of the sample, as well as for showing the complex stress histories at different cross sections. At impact, plane compression waves are produced in both the thin star-shaped flyer and the specimen (state 2). The reflection from the foam-flyer interface unloads the compressive wave, resulting in a compressive pulse of duration equal to the round trip travel time through the thickness of the star flyer. When the compressive pulse reaches the rear surface of the specimen, the gap between the specimen and the momentum trap plate produces a reflected wave which unloads the compressive pulse (state 3). Tensile stresses are generated after crossing the compressed region (state 4). By the time this pulse reaches the flyer-specimen interface, separation has taken place, and the pulse reflection causes compressive stresses (state 5). The initial compressive pulse, minus the pulse reflected at the gap, propagates into the momentum trap and reflects back. When this tensile pulse reaches the interface between the specimen and the momentum trap, the momentum trap separates since this interface cannot withstand tension. At this time the specimen is left unstressed and without momentum. Because of the impedance mismatch between the specimen and the momentum trap an additional compressive wave was reflected at the interface and made a round trip through the specimen. This, relatively small, compressive reloading occurred later than the principal loading of interest and is expected to have minor influence on the observed damage.

The above one dimensional analysis is valid in the central region of the specimen (Kumar and Clifton,

1977b), where the effects of diffracted waves from the corners and the edges of the flyer are minimized. The only cylindrical wave which passes through the central octagonal region is a shear wave, diffracted from the boundary upon the arrival of a cylindrical unloading wave at  $45^\circ$ . In order to fully assess the role of the cylindrical waves diffracted from the edges of the star, and the spherically diffracted waves from the corners of the flyer and the specimen, three dimensional elastic computations have been performed (Espinosa et al. 1991c). The principal unloading waves that travel in the central octagonal region are diffracted spherical waves emanating from the corners of the flyer. These waves produce tensile stresses within the sample. The maximum amplitudes of such stresses occur for transverse tensile stresses at the rear surface of the specimen. These amplitudes are of the order of 15% of the longitudinal compressive stress in the incident plane wave. It should be pointed out that this amplitude represents an upper bound for such stresses. First, in real experiments there is a lack of simultaneity for the time of contact of the eight corners, due to the tilt between the flyer and the specimen. Second, the divergence of the unloading waves from the corners will induce microcracking near these corners and thereby reduce the level of tensile stresses that propagate into the central octagonal region to a value below a fracture stress threshold. These features have been observed systematically in  $\text{Al}_2\text{O}_3$  and  $\text{AlN}/\text{AlN}/\text{Al}$  composite tested samples.

### 3.3 Experimental results

The velocity-time histories for two shots performed using this configuration are given in Fig. 10a and 10b. A summary of the experiments is given in Table II. Stresses for Shots 91-01 and 91-02 are stresses at the interface between the specimen and the momentum trap. The shear stress is the maximum shear stress. The stress-time his-

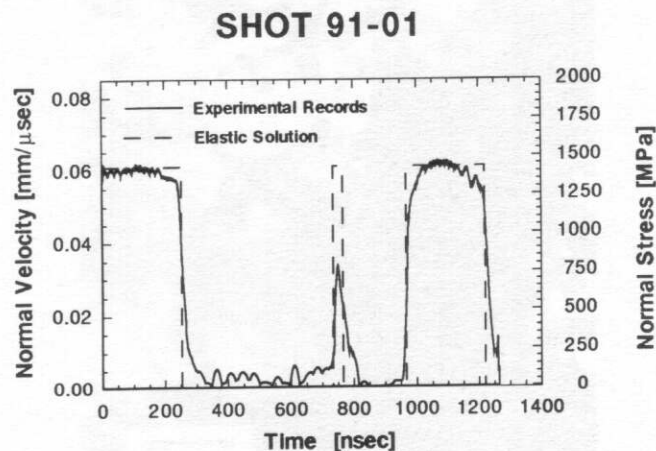


Figure 10a: Velocity-time profile for normal impact soft recovery experiment (Shot 91-01).



tories at the front surface of the momentum trap can be read from the secondary vertical axis. The predicted fully elastic solution is represented by dashed lines in the plot. This solution will be used as a point of reference for the discussion of several inelastic effects that are observed. The main compressive pulse, with durations between 240 and 195 nanoseconds, is followed by a second compressive pulse corresponding to the tensile pulse generated by an intentional gap of 30-90 nsec. The third pulse results from the reflection of the main pulse at the interface between the specimen and the momentum trap. Its close resemblance to the main pulse is an indication of the dominance of plane waves in the central

### SHOT 91-02

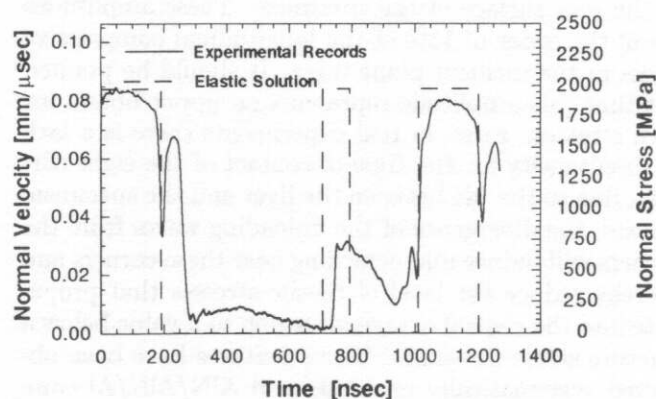


Figure 10b: Normal velocity-time profile for Shot 91-02. A strong spall signal and attenuation of the compressive pulse are observed.



Figure 11: High dislocation density encountered in the microstructure of recovered samples (Shot 91-02).

region of the sample. In the experiment at lower impact velocity, Shot 91-01, the compressive pulse has the full amplitude of the elastic prediction. This implies that initially the material did not undergo inelastic processes at this level of stresses; however, the small reduction in amplitude at the end of the pulse may be an indication of inelastic strain rates becoming significant. The tail at the end of the first compressive pulse appears to be the result of the inelastic strain rate that is produced by the nucleation and propagation of microcracks, see Fig. 10a. If so, the duration of the tail can be associated with the time required for the stress, at the wave front, to relax to the threshold value required for initiating crack propagation. Strong evidence of microcracking is found in the attenuation and spreading of the second compressive pulse. In Shot 91-02, stronger indications of inelasticity in compression appear towards the end of the pulse; this feature is consistent with the increase in dislocation density, within the AlN filler particles, the AlN reaction

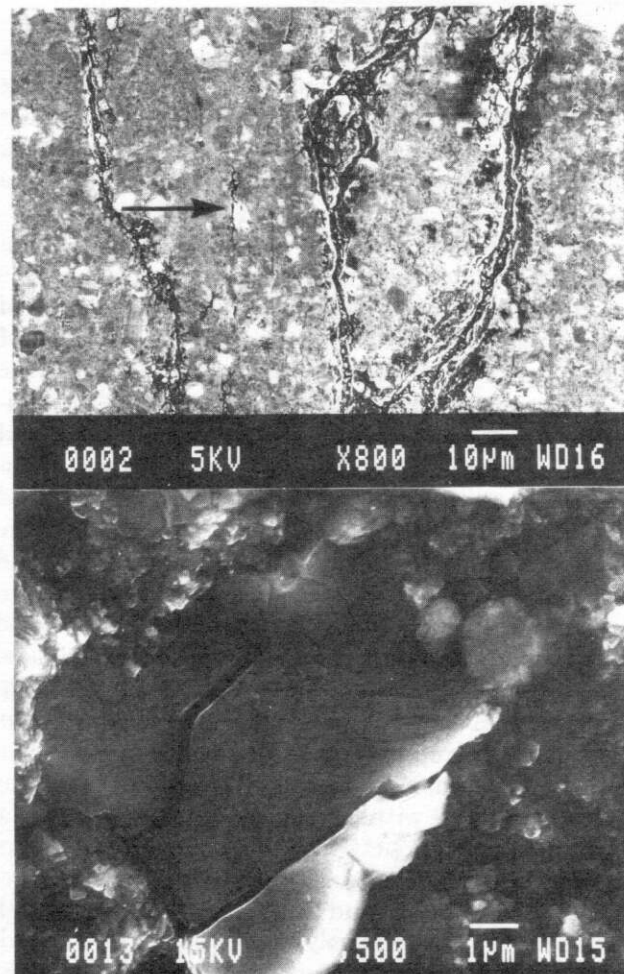


Figure 12: SEM micrograph of spall region perpendicular to the direction of wave propagation; a) Main cracks surrounded by isolated microcracks, b) Brittle failure of AlN filler particles.

product and the Al phase, observed in TEM samples made from the recovered specimens, see Fig. 11. Evidence of phase transformations (Rosenberg et al., 1991) or twinning, that are encountered at higher stress levels, was not found. In this shot a gap of 4  $\mu\text{m}$  was introduced by sputtering aluminum at the four corners of the momentum-trap plate. As a result, a tensile pulse with a duration of 85 nsec was produced. The magnitude and duration of this pulse is enough to cause the rapid development of a damage region, resulting in a spall signal at the end of the first compressive pulse. A scanning electron microscope (SEM) picture of this region is given in Fig. 12. Main cracks running perpendicular to the direction of wave propagation are observed, together with small cracks that did not coalesce. The spall strength at the onset of the process can be inferred from the unloading signal prior to the subsequent increase of the particle velocity. The time required for the formation of a spall plane is a function of the speed of the running cracks. The dynamic crack propagation in this case is governed not only by inertial effects but also by the plastic processes taking place along the wake of the

microcracks. Ductile ligaments that provide enhanced fracture toughness are observed in the SEM micrograph shown in Fig. 13. The attenuation and spreading of the second pulse is much more pronounced than in the case of Shot 91-01. Even if most of the attenuation occurs in the region where the pulse is tensile, state 4 in Fig. 1b, additional spreading and attenuation can be expected when the reflected compressive pulse traverses the damaged region, Fig. 12. Further delay in the return of the compressive pulse can result from the need to close an open spall crack before the stress is transmitted. Evidence of the latter behavior appears as delay, in the arrival of the second compressive pulse. From the free surface velocity measured at the beginning of the spall signal, calculation of the tensile stress at the spall plane indicates that the spall strength of this AlN/AlN/Al composite material is approximately 900 MPa.

#### 4. PRESSURE-SHEAR EXPERIMENTS

Normal impact experiments although valuable for providing direct means for assessing the validity of mathematical models of material response, have two major limitations. First, for a large class of hard materials, the compressive wave profiles are controlled primarily by the elastic compressibility of the material and not by the material softening or plastic flow. Second, the imposed stress trajectories for loading and unloading correspond to a straight line in the space of components of the stress deviator tensor. These two disadvantages can be overcome if the specimen is subjected to combined pressure-shear loading. Such loading is obtained by inclining the flyer and target to the axis of the projectile. A wide variety of non-proportional stress trajectories can be imposed by varying the angle of inclination. Limitations arise, particularly for ultra-hard materials, from sliding of the impact faces. This limitation can be reduced by increasing the roughness of the impacting surfaces. For roughness of the order of 0.2  $\mu\text{m}$  between peaks and valleys, angles of inclination up to 22° can be used without sliding. For the symmetric impact configuration, Fig. 3, the recorded wave profiles are determined by the inelastic response of the material through the thickness of the sample. Consequently the wave profile is attenuated and spread, and the strain rates are decreased. All field variables are strong functions of position and time.

The high strain rate pressure-shear configuration, Fig. 2a, offers some advantages over the symmetric impact configuration. One advantage of this experiment is that it allows the constitutive relation between stress, strain and strain rate to be obtained directly. High strain rates are obtained by impacting a thin specimen sandwiched between a hard flyer plate and a hard anvil plate. The flyer and anvil are designed to remain elastic up to the level of the imposed stresses. Because the flyer and anvil remain elastic, stresses, shear strain and strain rate

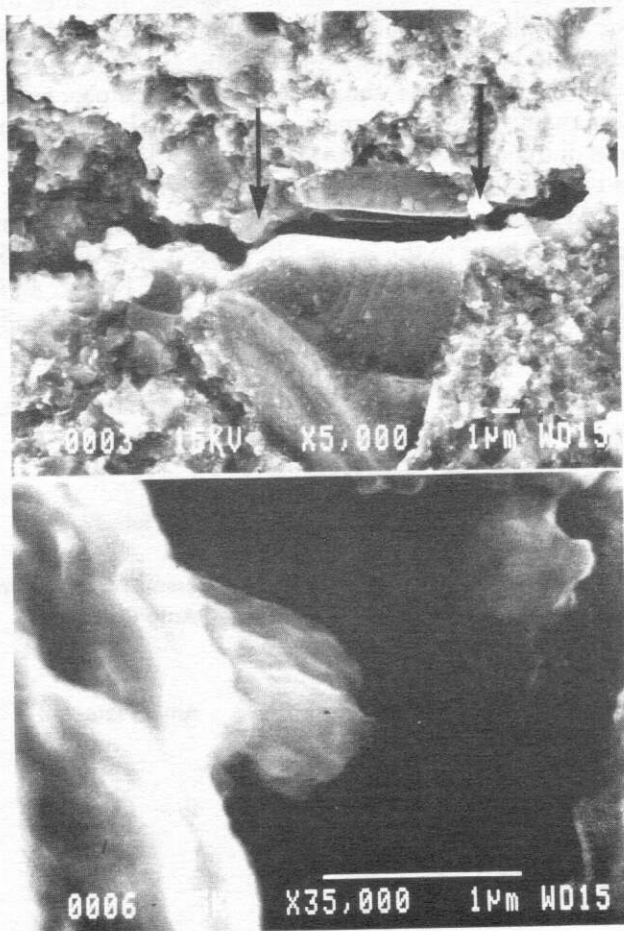


Figure 13: a) Ductile ligaments at the ends of a transgranular microcrack, b) Details of a ductile ligament bridging the crack faces.

can be obtained by measuring the transverse particle velocity at the rear surface of the anvil plate. The loci of stress and particle velocity for the anvil and flyer is given in Fig. 2b for the normal components and in Fig. 2c for the transverse components. Due to mismatch in longitudinal impedances, the normal stress in the sample increases, after each normal wave reverberation, until a homogeneous state of normal stresses is attained at which the normal stress has the value corresponding to the symmetric impact of the flyer and anvil, i.e.

$$-p = \sigma = \frac{1}{2} \rho c_1 u_0.$$

This stress level is reached because a finite difference in normal velocity, across the thickness of the sample, cannot be sustained in a state of uniaxial strain because of the resistance of the material to reduction in volume. In contrast, a finite difference in transverse velocity can be sustained across the thin sample. If the material deforms inelastically and the stress state is homogeneous, then the equilibrated shear stress corresponds to the flow stress of the material, see Fig. 2c. The strain rate is given by the velocity difference between the two faces of the sample divided by its thickness,

$$\dot{\gamma} = \frac{v_f - v_a}{h} = \frac{v_0 - v_{fs}}{h}$$

where  $v_0$  and  $v_{fs}$  are, respectively, the transverse components of the impact velocity and the velocity of the free surface of the anvil. The integration of the strain rate over time gives the shear strain,

$$\gamma(t) = \int_0^t \dot{\gamma} dt.$$

The shear stress is given by

$$\tau = \frac{1}{2} \rho c_2 v_{fs}.$$

These equations are used to construct the  $\tau$ - $\gamma$  curves at high strain rates and high pressures.

In the characterization of hard ceramics and composites, more demanding requirements are placed on the flyer and anvil plates. These plates must be hard enough in compression and shear to remain elastic at the high stress levels required for the inelastic deformation of the specimen, yet strong enough in tension to prevent failure at  $45^\circ$  when the shear wave propagates through the unloaded region adjacent to the rear surface of the anvil. These requirements have been met by using WC/6Co plates in shear and a tensile strength in excess of 1500 MPa.

Modified experimental configurations that provide information for different stress states or along different loading paths are also feasible. As an example, a pressure-change experiment is described in §4.4. Such a configuration is attractive for understanding the pressure dependence of the flow stress.

#### 4.1 General experimental procedure

The flyer plate is glued to the front end of a fiberglass tube with the impact plane skewed from the axis of the tube by an angle  $\alpha$ . An aluminum back with a rubber O-ring and a key is mounted in the rear end of the tube. The key of the projectile moves in the keyway of the barrel to prevent rotation of the projectile. The velocity of the projectile is measured just before impact by recording the times of contact of five wire pins placed in the path of the projectile. The measured projectile velocities are reported in table II.

The dimensions of the plates are chosen such that the first unloading wave from the periphery arrives at the point of measurement later than the unloading shear wave. The plates are lapped flat using a 12-inch lapping machine and 15  $\mu\text{m}$  boron carbide powder. In order to check their flatness, the plates were polished with 0.3  $\mu\text{m}$  alumina and placed under a monochromatic light source ( $\lambda=587.6 \text{ nm}$ ). Fewer than two fringes were observed. Before the test, the two impact surfaces were lapped with 15  $\mu\text{m}$  diamond paste to provide sufficient surface roughness to transfer the in-plane motion without sliding.

After the target plate is mounted in the holder ring, it is aligned to the face of the projectile within 0.05 milliradians using a technique introduced by Kumar and Clifton, 1977a, fig. 14. In order to check the angle of

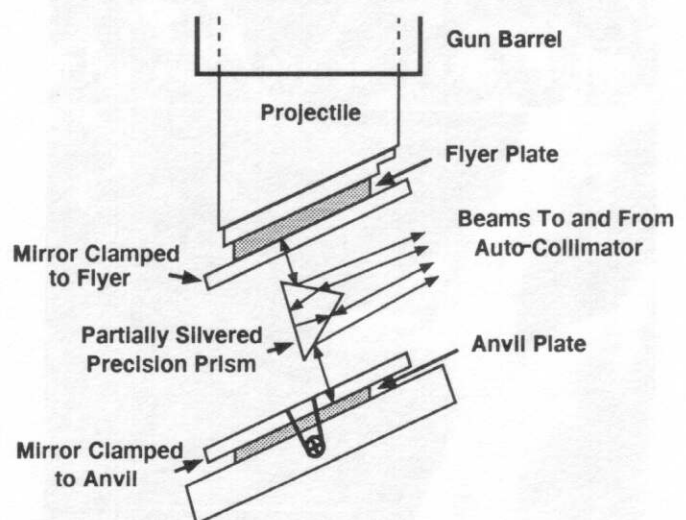


Figure 14: Schematic layout of alignment technique.



misalignment at impact, the times of contact is recorded at four voltage-biased pins as discussed previously.

The normal and transverse component of the motion of a point on the rear surface of the target are monitored by means of a Normal Velocity Interferometer (NVI) and a Transverse Displacement Interferometer (TDI). A schematic of the optical measuring system is shown in fig. 15. The specimen rear surface was polished and then a thin layer of positive photoresist was deposited using a spinning machine. A phase grating was constructed by interference of two laser beams. By changing the beam angles, phase gratings with sinusoidal profiles up to 700 lines/mm have been made. For the case of non-reflective materials, like the AlN/AlN/Al composite material, a thin film of aluminum was sputtered *a posteriori*.

The zeroth order reflected beam is used to monitor the normal velocity, using the NVI introduced by Barker and Hollenbach, 1965. The returning beam is split into two beams at the beam splitter BS<sub>2</sub>, Fig. 15. One of these beams travels through a delay leg, before the two beams are recombined at BS<sub>3</sub>. The interference between the recombined beams gives a measure of the motion of the rear surface of the target. A peak to peak variation in the intensity corresponds to a velocity change  $\lambda/2\tau$ , where  $\tau$  is the time required for the laser beam to propagate around the delay leg. For times less than  $\tau$

after arrival of the normal wave, the interferometer corresponds to a NDI as discussed by Clifton, 1970. This feature has been considered in the data reduction in order to obtain the velocity jump. The TDI, developed by Kim, Clifton and Kumar, 1977, makes use of two *n*th order diffracted beams which are recombined at the BS<sub>1</sub>. When the rear surface of the target plate moves transversely, the two selected diffracted beams are Doppler-shifted inducing a phase change in the diffracted beams. When these beams are mixed, beating takes place at a frequency proportional to the transverse velocity. The transverse displacement or sensitivity of the TDI is  $d/2n$   $\mu\text{m/fringe}$ , where  $d$  is the pitch of the diffraction grating and  $n$  is the diffraction order of the chosen beams.

#### 4.2 Pressure-shear symmetric impact results

The output of the LeCroy oscilloscope for Shot 91-03, is given in Fig. 16. For the TDI trace, the arrival of the shear wave corresponds to the time at which the high frequency oscillations begin. The earlier oscillation (less than two periods) results from transverse motion associated with the inclination of the longitudinal wave to the rear surface. Such inclination can result from the lack of perfect parallelism of the two faces of the anvil plate. Variations in intensity in the TDI trace, thought to be due to rotation of the grating plane caused by inhomogeneous inelastic deformation of the sample, do not

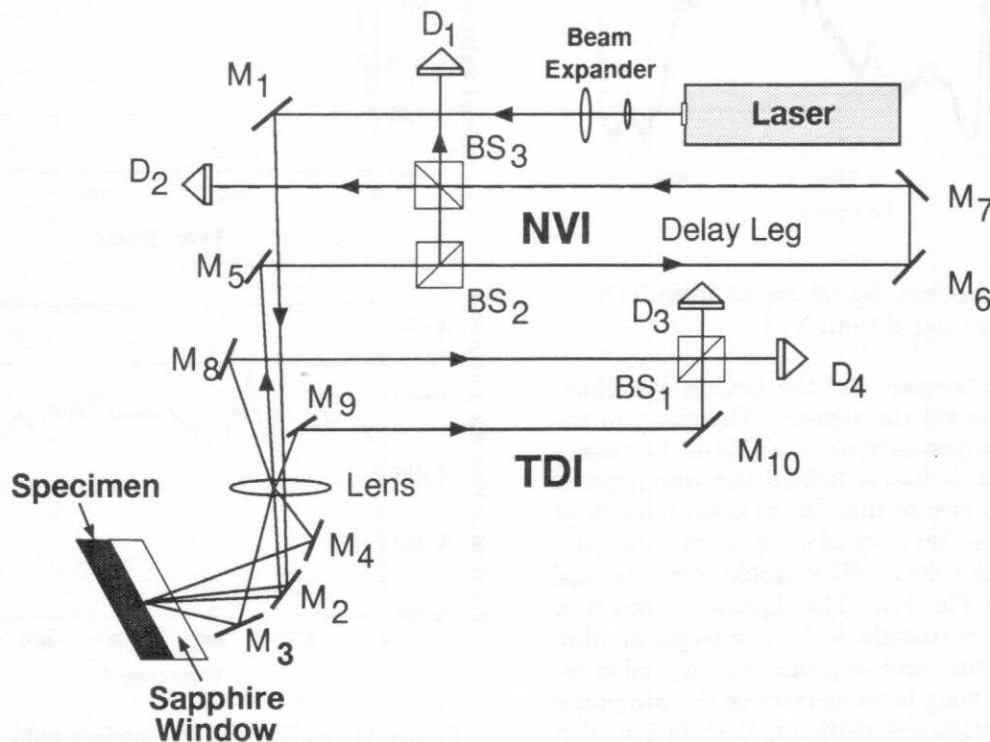


Figure 15: Optical layout of combined NVI-TDI interferometers.

appear to be so pronounced as to interfere with the interpretation of the transverse displacement. The NVI trace starts with a straight line which corresponds to the time before any disturbance arrives at the rear surface of the target. When the elastic precursor of the longitudinal wave arrives, the trace shifts abruptly, followed by a burst of fringes. For times less than the delay leg time  $\tau$  (i.e. 8.507 ns) the NVI corresponds to a Normal Displacement Interferometer (NDI). The frequency of the fringes during this time may exceed the

Fluctuations observed during the time of interest are due in part to errors in data reduction arising from the insensitivity of the TDI at the peaks and valleys of the traces. The reduced level of the shear stress can be due to (i) slip at the impact plane, (ii) plastic flow, and (iii) tensile fracture on planes at  $45^\circ$  in the state of pure shear that arises after the unloading of the compressive wave (see Fig. 3). Because of the small skew ( $18^\circ$ ) of the impacting plates, the possibility of sliding appears to be unlikely. Moreover, since the tensile strength, measured in the soft-recovery experiments is approximately 900 MPa, the third possibility appears to be unlikely. If plastic flow occurs, then the limiting shear stress is approximately 460 MPa. In order to clarify these matters, two other pressure-shear configurations have been used: symmetric pressure shear with the addition of a sapphire window to prevent the development of a state of pure shear upon unloading of the longitudinal wave, and high strain rate pressure shear under conditions which ensure normal compressive stresses while the shearing resistance is monitored.

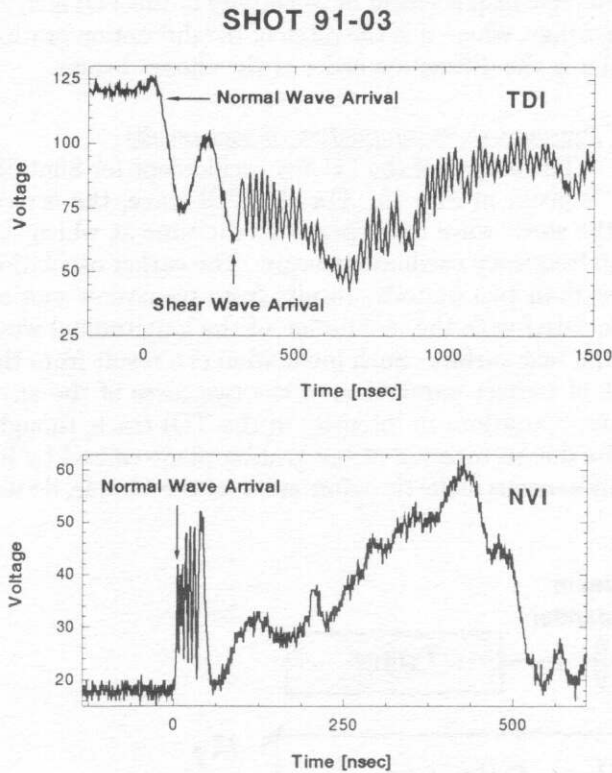


Figure 16: a) LeCroy digital signal from TDI, b) LeCroy digital signal from NVI.

maximum response frequency of the LeCroy Waveform Digitizer used to record the signals. Therefore, in the data reduction an adjustment of the value of the normal particle velocity, immediately behind the wavefront, is allowed in order to ensure that the plateau velocity at later times is equal to the normal component of the projectile velocity. The velocity-time profile of the normal motion is shown in Fig. 17a. The risetime, which is of the order of 50 ns, is thought to be due to plastic flow of the aluminum phase and to geometric dispersion associated with the strong heterogeneity of the composite material. The principal observation is that, in Fig. 17b, the shear stress is approximately constant, throughout the measured interval, at a level less than that expected for elastic response (showed as a horizontal dashed line).

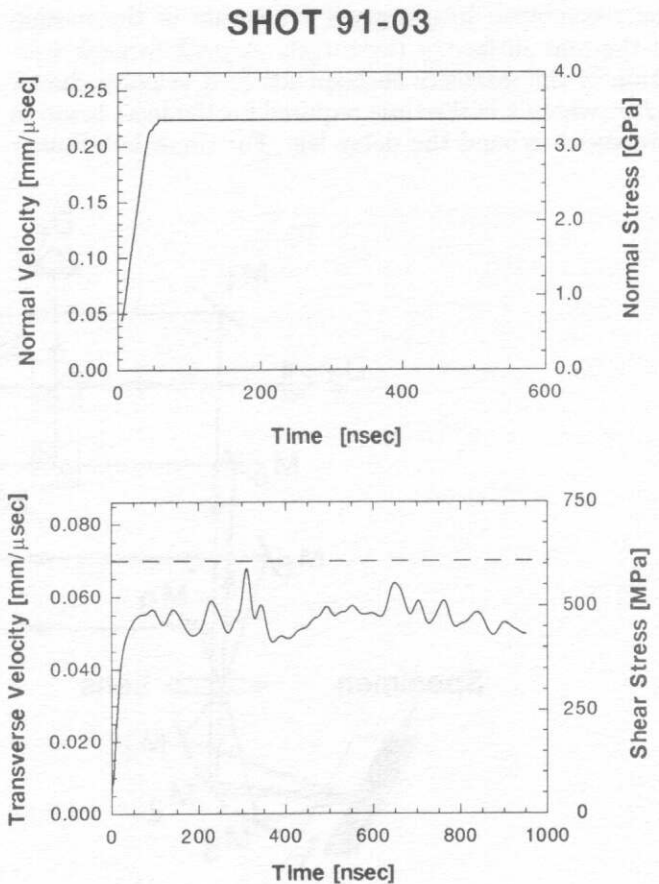


Figure 17: a) Normal free surface velocity-time for symmetric pressure-shear impact, b) Transverse free surface velocity-time for symmetric pressure-shear impact.

#### 4.3 Pressure-shear sandwich configuration results

In Shot 91-05, the AlN/AlN/Al composite specimen was sandwiched between two WC/6Co plates. The normal velocity-time profile corresponding to this shot, is shown in Fig. 18a. The reduction in particle velocity after the initial jump indicates the presence of a small gap at the AlN/AlN/Al-WC/6Co interface in the flyer assembly. While this gap can be completely eliminated for soft metal specimen by means of diffusion bonding, Tong W., 1991, the scenario is much more complicated for the case of hard materials. However, since the interest in the experiment is in the state of homogeneous deformation that develops after the transient state, the existence of a gap of a few microns does not appear to affect the interpretation of the experimental records. The velocity rise upon the closure of the gap is associated with the reverberation of waves within the specimen. This part of the data corresponds to a non-homogeneous deformation state and cannot be used directly for the characterization of the material properties. The normal particle velocity rises ultimately to the value predicted by the elastic impact of AlN/AlN/Al composite material against the WC/6Co anvil. The transverse particle velocity, given in Fig. 18b, follows a history similar to that observed for the normal stress. Thus, at least during the transient time, the frictional behavior at the impact surfaces dominates the shear response. After the sudden drop in transverse velocity, the shear stress rises and stays nominally constant for 800 nsec. Some peaks and valleys in the transverse velocity history are observed, that appear to be too large to be attributed to the data reduction process. The  $\tau$ - $\gamma$  curve, obtained using the equations discussed at the beginning of the section, is given in Fig. 18c; in plotting this curve, no strain accumulation is assumed to occur during the unloading and reloading caused by the gap. A finite shear strain of 13% was measured.

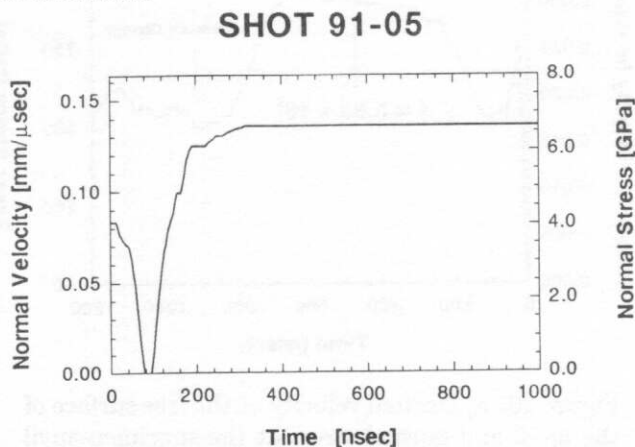


Figure 18a): Normal velocity at the free surface of the anvil and normal stress at the specimen-anvil interface.

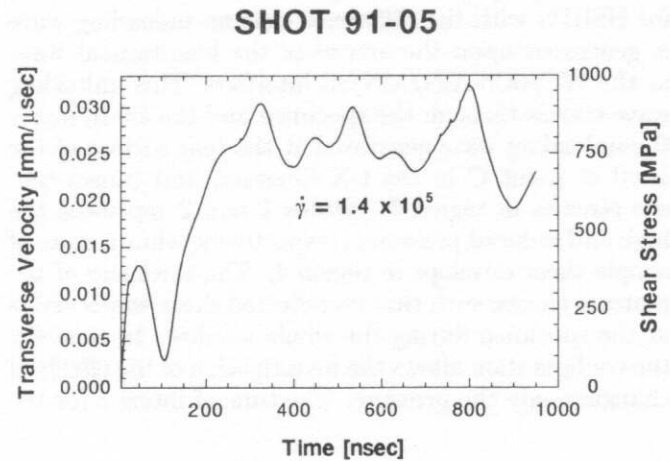


Figure 18b): Transverse velocity at the free surface of the anvil and shear stress at the specimen-anvil interface.

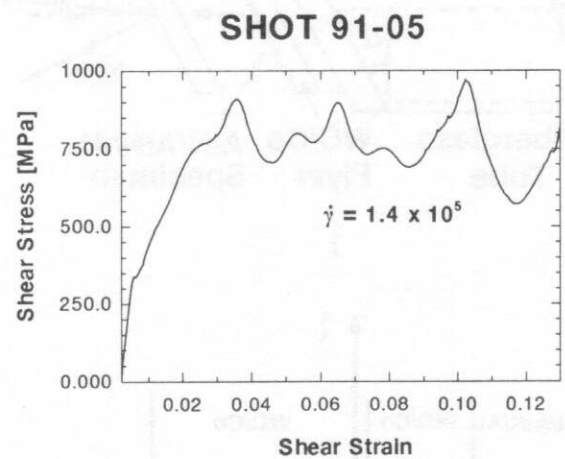


Figure 18c): Dynamic shear stress-strain curve at a hydrostatic pressure of 6.59 GPa.

#### 4.4 High strain rate pressure-change results

In order to rule out the possibility of sliding, a test with an angle of inclination of  $15^\circ$  was conducted. In addition, the configuration was modified to produce a pressure change in the center of the shear window. The schematic of the test together with the t-X diagram is shown in Fig. 19. The change in pressure is achieved by introducing a double-plate flyer consisting of a high impedance, hard plate, e.g. WC/6Co, backed by a low impedance, hard plate. In this study the same AlN/AlN/Al composite material has been used as a back plate. The thin specimen is attached to the flyer and is sandwiched between the flyer and the anvil as in the high strain rate pressure shear configuration (HSRPS).



The wave propagation analysis is very similar to that for HSRPS with the difference that an unloading wave is generated upon the arrival of the longitudinal wave at the WC/6Co-AlN/AlN/Al interface. This unloading wave travels through the specimen and the anvil, meets the unloading wave generated at the rear surface of the anvil at point C in the t-X diagram, and causes tensile stresses in region 5. States 1 and 2 represent the high and reduced pressures, respectively, while a state of simple shear develops in region 4. The thickness of the plates is chosen such that no reflected shear waves arrive at the specimen during the whole window. In this way the configuration allows the investigation of the effects of changing only the pressure. The time of interest for the

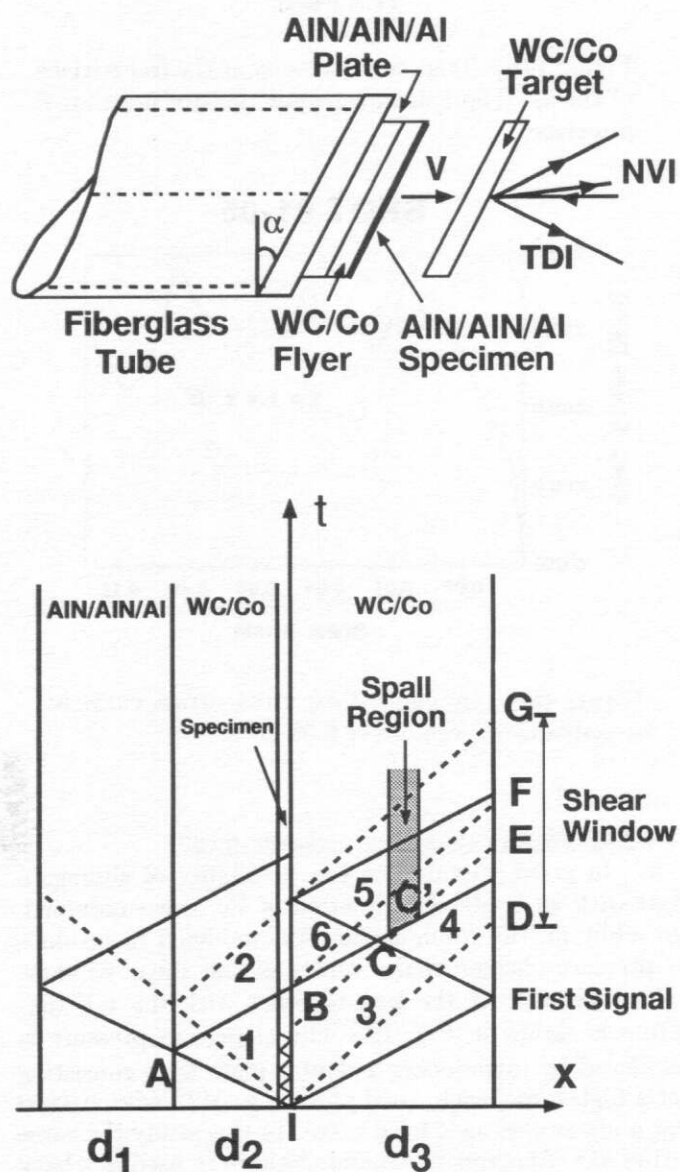


Figure 19: Schematic of high strain rate pressure change experiment and corresponding t-X diagram.

shear response is the time between points D and G in the diagram. For the experiment to be successful, the interface between the two different impedance plates should not have a gap that would fully unload the normal stress. If such unloading were to occur, microcracks may be generated in the specimen due to residual stresses developed by plastic deformation gradients within the microstructure. Diffusion bonding of the AlN/AlN/Al back-up plate to the WC/6Co plate has been done by sputtering a thin copper film 2  $\mu\text{m}$  thick onto the WC/6Co plate. Bonding was obtained by applying a pressure of 100 MPa at 550°C in a vacuum environment for a period of 30 minutes.

The normal and transverse velocities recorded for Shot 91-06 are given in Figs. 20a and 20b, respectively. The main features of the records for the first 700 nsec. are very similar to those discussed previously for Shot 91-05. The main difference is in the shear stress measured at the homogeneous state of deformation. The strain rate, as reported in table II, is of the same order

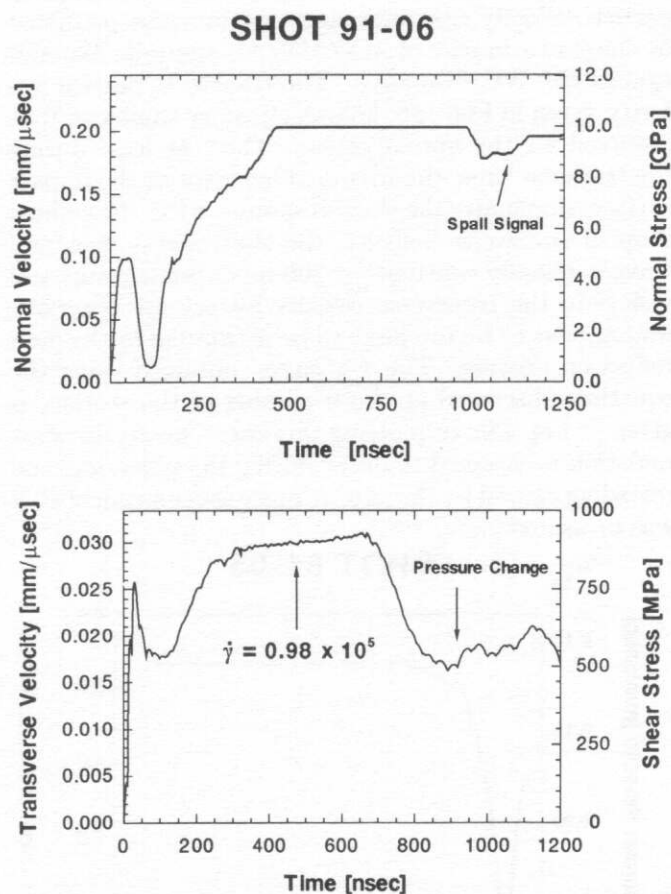


Figure 20: a) Normal velocity at the free surface of the anvil and normal stress at the specimen-anvil interface. b) Transverse velocity at the free surface of the anvil and shear stress at the specimen-anvil interface.

of magnitude for both tests. An increase of the order of 90% in pressure results in an increase of 10% in the flow stress. From the previous description of the microstructure and the TEM micrographs showing the AlN filler particles surrounded by a matrix composed of submicron grains of AlN reaction product and Al alloy, the origin of this pressure sensitivity appears to be in the kinematics of the deformation process. For the material to sustain finite deformations in shear, the hard AlN filler particles have to rotate and translate relative to each other with plastic deformation and damage localized in the AlN reaction product and Al alloy phase. By considering the obstacles that each filler particle has to overcome in its relative motion, it may be possible to rationalize the importance of the normal stress.

The analysis of the shear stress history reveals that a decrease in transverse particle velocity is recorded before the reduction in pressure. By examining carefully the different possibilities that can cause this reduction, one concludes that spalling of the WC/6Co took place as a result of the tensile normal stresses generated in the anvil plate, region 5 in the  $x$ - $t$  diagram given in Fig. 19. The position of the spall region, point C', is governed by the loading rate at the impact surface. As mentioned previously, the normal stress increases with the wave reverberations within the sample and its rate of increase is a function of the plastic behavior of the specimen. The increase in the normal particle velocity, after the arrival of the unloading wave, i.e. approximately at 1  $\mu$ sec, shows a clear picture of spalling.

The unloading wave which is generated at the rear surface of the anvil plate and which is the cause of the observed spalling, can be eliminated by the use of the window interferometer described in the next section. This modification would allow the measurement of the evolution of the flow stress as a function of pressure change in a single experiment.

## 5. PRESSURE-SHEAR IMPACT WITH WINDOW INTERFEROMETRY

Several research efforts have been made for *in-material measurements* of longitudinal and shear waves in impacted solids. Gupta Y.M., 1976 and Gupta et al., 1980, reported successful experiments where velocity profiles have been obtained at interior surfaces by inserting metallic gauges in a magnetic field and measuring the current generated by their motion. This technique can be applied only to nonmetallic materials. Moreover, for the measurement of pure compression and pure shear profiles, two experiments with identical configuration and projectile velocity are needed. The other technique developed for in-material measurements, Williams and Keough, 1968, Rosenberg and Bless, 1986, Bless et al., 1987, employs manganin gauges placed between the

specimen back face and a thick PMMA disk to measure the time history of the longitudinal stress  $\sigma_1$ . The measurement of the transverse stress,  $\sigma_2$ , is accomplished by placing another manganin gauge at an interface made in the direction of wave propagation. The shear stress is obtained as the difference between the two normal stresses,  $\sigma_1$  and  $\sigma_2$ . A major concern with this technique is the perturbation of the one dimensionality of the wave propagation due to the presence of a thin layer, perpendicular to the wave front, filled with a material having a different impedance. Calculations by Wong and Gupta, 1991, show that the inelastic response of the material being studied affects the gauge calibration; consequently, calibration on the basis of low-velocity elastic shots appears to be inadequate.

The direct measurement of displacements (NDI, TDI) and particle velocities (NVI) together with the precision of laser-beam interferometry (2-3 nsec resolution), has resulted in accurate dynamic characterization of solids. The technique presented here is an extension, to the case of combined normal and shear motion, of the window interferometer introduced by Baker and Hollenbach, 1970. It can be used for both of the techniques that produce pressure-shear loadings: oblique impact and impact with anisotropic crystals such as Y-cut quartz, (Chhabildas L. and Swegle J., 1980). Since the technique does not require special modifications of the plate impact facilities, it can be applied easily in most shock-wave laboratories.

Pressure-shear impact with window interferometry presents several advantages over the other techniques mentioned previously. No interfaces are required that can perturb the one dimensionality of the wave propagation. The method can, in principle, be used for a wide range of materials. The measurement of both the longitudinal and shear waves are made at the same spatial point with a time resolution of approximately 2-3 nanoseconds. In addition, the method conserves the fundamental advantage that the measured wave profiles are undisturbed by reflections of the compressive wave at free surfaces.

### 5.1 *Elastic wave propagation analysis*

The elastic wave fronts for a plane wave analysis are given in the Lagrangian  $t$ - $X$  diagram in Fig. 21. At impact, plane compression waves and shear waves are produced in both the impactor and the specimen. In the absence of a gap at the specimen-window interface, the major part of the compressive pulse propagates into the window and the remainder is reflected due to a small mismatch in impedances. A reflected tensile pulse is generated when the transmitted compressive pulse reaches the free surface of the window. When this tensile pulse arrives at the specimen-window interface, slippage can take place due to the strong reduction in normal stress and therefore useful information on the shear wave is limited.

ited to times less than the time corresponding to point E in Fig. 21.

Similar features are encountered in the history of the shear wave. The propagating shear wave develops a state of pure shear, within the window material, in region 4 of the t-X diagram.

## 5.2 General experimental procedure

Sapphire has been chosen as the window material because it remains transparent up to normal stresses of 15 GPa. It has an impedance that matches many ceramics and ceramic composites. Its spall strength is closed to the Hugoniot elastic limit (HEL), which is of the order of 20 GPa in the Z direction. Because this stress is considerable larger than the stresses encountered in the experiments reported here, difficulties arising from

yielding of the window material in the interpretation of the experimental records are not expected. Such difficulties are encountered when Lithium Fluoride is used as a window material and high impact velocities are used, see e.g. Kipp M. and Grady D., 1989.

For the experiment to be successful the specimen-window interface should transmit the in-plane motion without damage or plastic flow. In addition, a grating that can generate the necessary diffracted beams for the measurement of transverse velocities is required. The design of the multi-layer tailored interface given in Fig. 22e meets both of these requirements. The grating is a Ronchi ruling made of Ti strips. Fig. 22a-e summarizes the steps involved in its manufacturing. The process starts with the sputtering of a Ti layer 1000Å thick. Then, by using standard photolithographic techniques a photoresist mask 1µm thick is constructed with the desired pitch. The exposed Ti is etched by using an etchant with the composition: dist. water 100 ml, hydrofluoric acid (40%) 1 ml and nitric acid 2 ml (Kroll's reagent). Alternatively, reactive ion etching (RIE) using  $\text{CF}_4 + 8\% \text{O}_2$  successfully etched Ti with the following parameters: RF power per unit area = 0.4 W/cm<sup>2</sup>,

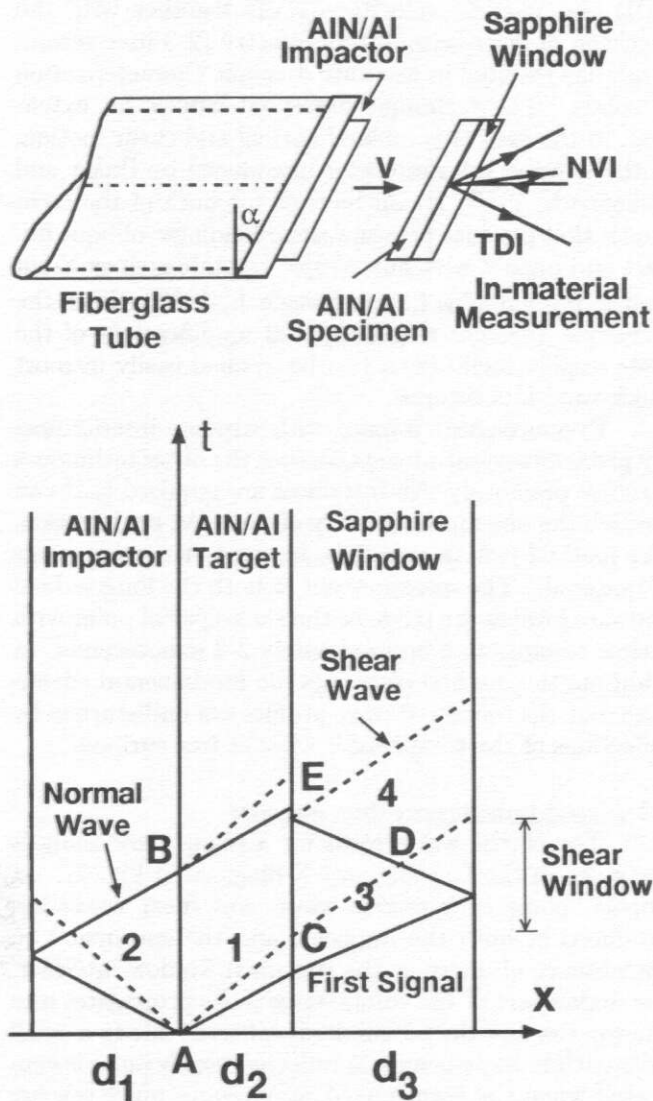


Figure 21: Schematic of pressure-shear impact with window interferometer and corresponding t-X diagram.

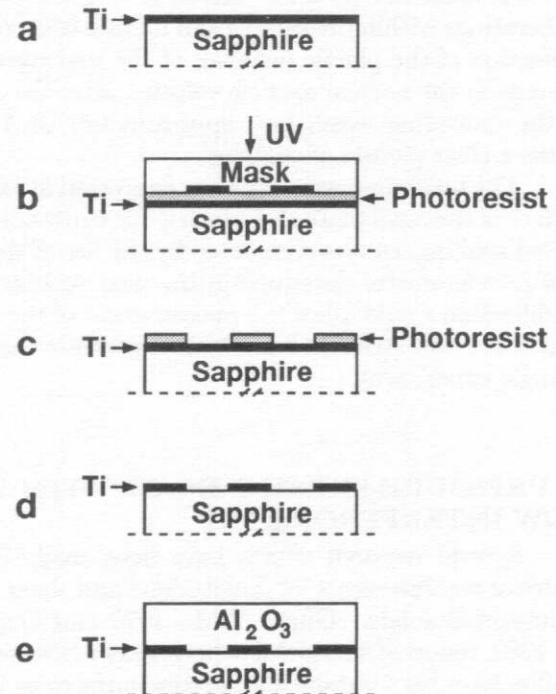


Figure 22: Illustration of interface preparation procedure: a) Sputtering of Ti thin film, b) Deposition and developing of grating pattern on photoresist, c) Reactive ion etching of Ti, d) Remotion of patterned photoresist, e) Sputtering of  $\text{Al}_2\text{O}_3$  thin layer.



Bias voltage=560 V, total chamber pressure=20 mT, CF<sub>4</sub> flow rate= 37 sccm, O<sub>2</sub> flow rate= 3 sccm and Dwell time=1.2 sec. This dry etching method should be preferred for the manufacturing of submicron gratings.

The selection of the Ti thin film as the reflecting part of the grating is based on its strong adhesion to sapphire. Peel tests conducted by Kim Y., et al., 1987, show that Ti deforms plastically when it is bonded to sapphire substrates. This behavior was rationalized by the elastic properties of the substrate and the chemical reaction at the interface where the oxygen present in the sapphire microstructure contributes to the formation of a TiO<sub>2</sub> transition film.

After removing any remnant photoresist, an Al<sub>2</sub>O<sub>3</sub> layer with thickness between 10-15  $\mu\text{m}$ , is sputtered onto the sapphire substrate containing the diffraction grating. Al<sub>2</sub>O<sub>3</sub> thin films of high quality, characterized by their transparency, adhesion to the substrate, layer uniformity and good stoichiometry, have been obtained. The parameters used were, RF power= 5 W/cm<sup>2</sup>, chamber pressure= 30 mT and a distance between the Al<sub>2</sub>O<sub>3</sub> target (99.99% purity) and the sapphire substrate of 1.4 inches. The rate of deposition was 200  $\text{\AA}/\text{min}$ . In order to avoid cracking due to the generation of thermal stresses in the substrate and target, both target plate and the window plate were maintained at room temperature by a cooling capability incorporated in the design of the machine.

The frictional properties of the specimen-window interface are exploited to transmit the in-plane motion. Neither epoxy nor alumina-filled epoxy are used to bond the specimen to the sapphire window because they strongly limit the level of shear tractions that can be transmitted to the window. Furthermore, the frictional requirements at the interface are less stringent than at the impact surfaces, because the pressure wave arrives before the shear wave. To meet these requirements, the Al<sub>2</sub>O<sub>3</sub> thin film on the sapphire window, is lapped to a flatness better than 2 Newton rings (under monochromatic light  $\lambda=587.6 \text{ nm}$ ) and its roughness increased by using 15  $\mu\text{m}$  boron carbide powder. The specimen and window plates are assembled in a clean room. After they are clamped together, small amounts of epoxy are applied at the edges.

The compression and shear wave behavior is recorded by monitoring the time resolved motions of the ceramic-sapphire interface with normal velocity and transverse displacement interferometric techniques (NVI and TDI), Fig. 15. The measurements are recorded on a transient digital oscilloscope LeCroy Waveform Digitizer with a sampling period of 0.742 nsec per data point. The interference fringes measured with the TDI are first filtered by using a Fast-Fourier Transform method. The filtered amplitudes of the fringes are then scaled to obtain uniform fringe amplitude. By numerical differentiation,

the transverse velocity versus time profile is obtained. Details of the data reduction process can be found in Tong W., 1991.

Similar data processing is used for the NVI, Zhou M. and Clifton, 1991, except that differentiation is not required. However, the relationship between the number of fringes and the particle velocity being measured must be changed to account for the refractive index of the window. Before the longitudinal wave reaches the free surface of the window this relationship is (Setchell R., 1979)

$$u(t - \frac{\tau}{2}) = \frac{\lambda F(t)}{2\tau n_1} - c_1 \frac{(n_1 - n_0)}{n_1}$$

where  $F(t)$  is the number of fringes,  $\lambda$  is the wavelength of the laser light,  $\tau$  is the delay time,  $n_0$  is the refractive index of the unstressed window material,  $n_1$  is the refractive index in the stressed material, and  $c_1$  is the longitudinal wave speed. The form of the equation for the particle velocity can be related to the form given by Baker and Hollenbach, 1970. They have calibrated the sapphire window for laser interferometry by performing symmetric elastic tests. Their calibration results are used for the interpretation of the experimental records.

### 5.3 Experimental results

Time resolved velocity profiles for Shot 91-04, corresponding to the normal and in-plane components of the motion are displayed in Figs. 23a and 23b, respectively. The compressive wave shows a jump in particle velocity followed by a ramp-wave structure. This profile is consistent with an initial elastic limit followed by a dynamic hardening region; however, the ramp may also be associated with closure of rough surfaces at the specimen-window interface.

The shear wave shows a similar structure in the first 30 nsec. The amplitude predicted for elastic response is attained. A decreasing shear stress is observed at later times that is characteristic of wave attenuation due to inelastic strain rates developing behind the wave front. The peak shear stress is  $\tau = 750 \text{ MPa}$ , which is below the maximum shear stress measured in Shots 91-05 and 91-06 but consistent with the lower shear stress expected because of the lower normal stress and the evidence of pressure-sensitivity of the flow stress.

The same experimental configuration has been used successfully for conducting a test addressing the reduction in shear strength in alumina (Espinosa et al., 1991d). The experimental records show that even after compressive wave attenuation the shear strength remains essentially unchanged for the level of stresses examined. The shear wave amplitude also exhibits an attenuation similar to the one reported in Fig. 23b for AlN/AlN/Al composite material. These features suggest the inade-

quacy of the Hugoniot elastic limit as a measure for the characterization of the threshold for inelastic deformation in ceramics.

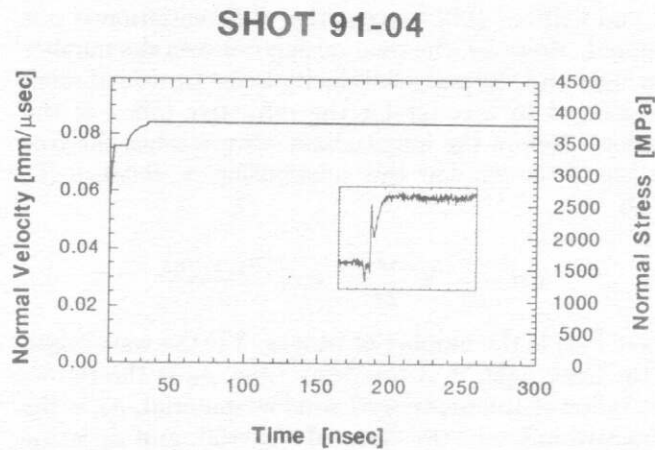


Figure 23a: Normal particle velocity as a function of time measured at the specimen-sapphire interface.

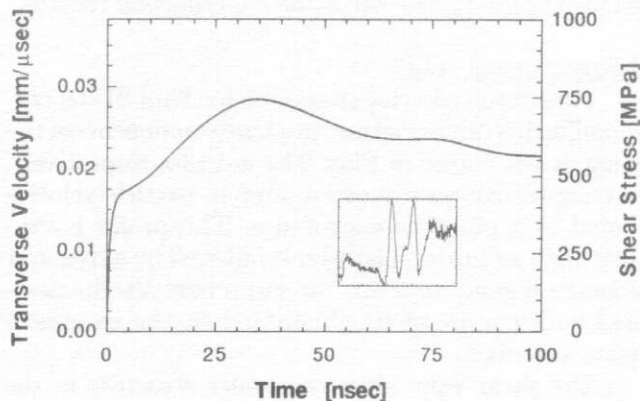


Figure 23b: Transverse particle velocity-time measured at the specimen-sapphire interface.

#### 5.4 *Application to related research*

The methodology presented here opens several possibilities for fundamental studies of micromechanics of inelastic deformation and damage in solids. The technique allows the measurement of transverse particle velocities at a range of distances from the impact surface, including positions that are very close to the impact surface. By placing the point of observation at different depths within the material, direct determination of shear stress-time histories can be obtained. This feature is of great interest for clarification of the reported strong reduction in shear strength together with the development of failure waves in glasses, Bless et al., 1991. The

approach should also be valuable in understanding the complex wave structure that arises in solids undergoing phase transformations.

Since by using lithographic methods and thin film technology, it is possible to produce crack-like defects of controlled size and position along interfaces, the micromechanical study and field characterization of dynamic failure of metal-ceramic interfaces containing tailor-made microdefects should be feasible. Use of a multi-point TDI should facilitate the interpretation of the details of crack initiation and propagation.

#### CONCLUDING REMARKS

Plate impact has been shown to be quite versatile in providing data on the response of a high strength composite under loading conditions which are severe enough to cause inelastic deformation and damage, yet simple enough to allow relatively straightforward interpretation. The soft-recovery and pressure-shear configurations are complementary in the sense that the former allows for the microscopic examination of damage mechanisms whereas the latter allows the measurement of macroscopic flow stresses and tensile strength under a variety of well-characterized dynamic loading conditions. Although only a few experiments were conducted on the composite material consisting of AlN particles in an AlN/Al matrix, these experiments are sufficient to establish that the yield stress in pure shear is approximately 450 MPa and that at strain rates of the order of  $10^5 \text{ s}^{-1}$  a flow stress of approximately 780 MPa develops at normal pressures of 6.7 GPa. This flow stress increases to approximately 875 MPa at normal pressures of 10 GPa. The spall strength of the composite is approximately 900 MPa.

#### ACKNOWLEDGMENTS

This research was supported by the National Science Foundation through its support of the MRG on Micromechanics of Failure-Resistant Materials. We acknowledge the support of Lanxide Armor Products, Inc. in providing the AlN/AlN/Al composite material samples. We appreciate the contributions of Prof. Steven Nutt of Brown and Kathy Leighton of Lanxide in the interpretation of the SEM and TEM micrographs. We are grateful to Roland Beaulieu for useful discussions and for performing the thin film depositions. We thank William Patterson for providing technical insight during the RIE tests, and Michael Mello for overall assistance in the plate impact experiments.

## REFERENCES

- Abou-Sayed, A.S. and Clifton, R.J., 1976, "Pressure Shear Waves in 6061-T6 Aluminum due to Oblique Impact," *J. Appl. Mech.*, Vol. 44, Trans. ASME, Vol. 99, pp. 85-88.
- Barker, L.M. and Hollenbach, R.E., 1965, "Interferometer Technique for Measuring the Dynamic Mechanical Properties of Materials," *Rev. Sci. Instrum.*, Vol. 36, pp. 1617.
- Barker, L.M. and Hollenbach, R.E., 1970, "Shock-Wave Studies of PMMA, Fused Silica, and Sapphire," *J. Appl. Physics*, Vol. 41, p. 4208.
- Bless, S.J., Brar, N.S., and Rosenberg, Z., 1987, "Strength of Soda Lime Glass Under Shock Compression," *Proceedings of 1987 APS Topical Conference on Shock Waves in Condensed Matter*, pp. 309-312.
- Bless, S.J., Brar, N.S., Kanel, G., and Rosenberg, Z., 1991, "Failure Waves in Glass," *Private Communication*.
- Chhabildas, L.C. and Swegle, J.W., 1980, "Dynamic Pressure-Shear Loading of Materials Using Anisotropic Crystals," *J. Appl. Physics*, Vol. 51, p. 4799.
- Clifton, R.J., Raiser, G., Ortiz, M. and Espinosa, H.D., 1990, "A Soft Recovery Experiment for Ceramics," *Proc. of 1989 APS Conf. on Shock Compression of Condensed Matter*, pp. 437-440.
- Clifton, R.J. and Klopp, R.W., 1985, "Pressure-Shear Plate Impact Testing," *Metal Handbook*, Vol. 8, 9<sup>th</sup> Edition, pp. 230-239.
- Clifton, R.J., 1970, "On the Analysis of the Laser Velocity-Interferometer," *J. Appl. Physics*, Vol. 41, pp. 5335-5337.
- Creber, D.K., Poste, S.D., Aghajanian, M.K. and Claar, T.D., 1988, "AlN Composite Growth by Nitridation of Aluminum Alloys," *J. Ceram. Eng. Sci. Proc.*, Vol. 9, pp. 975-982.
- Espinosa, H.D., Ortiz, M. and Clifton, R.J., 1991a, "Micromechanics of Ceramic Materials: Modeling," in preparation.
- Espinosa, H.D., Raiser, G., Clifton, R.J. and Ortiz, M., 1991b, "Inelastic Mechanisms in Dynamically Loaded Ceramics," *Conf. Proc. ASCE*, Columbus, OH.
- Espinosa, H.D., Raiser, G., Clifton, R.J. and Ortiz, M., 1991c, "Performance of the Star-Shaped Flyer in the Study of Ceramic Materials, Three Dimensional Computer Simulations and Experimental Observations," in preparation.
- Espinosa, H.D., Clifton, R.J. and Ortiz, M., 1991d, "Micromechanics of Ceramic Materials: Microscopy Study and Pressure Shear Experiments," in preparation.
- Gilat, A. and Clifton, R.J., 1985, "Pressure-Shear Waves in 6061-T6 Aluminum and Alpha-Titanium," *J. Mech. Phys. Solids* 33, pp 263-284.
- Gupta, Y.M., 1976, "Shear Measurements in Shock Loaded Solids," *Appl. Phys. Lett.*, Vol. 29, pp. 694-697.
- Gupta, Y.M., Keough, D.D., Walter, D.F., Dao, K.C., Henley, D., and Urweider, A., 1980, "Experimental Facility to Produce and Measure Compression and Shear Waves in Impacted Solids," *Rev. Sci. Instrum.*, Vol. 51(a), pp. 183-194.
- Hagege, S., Ishida, Y. and Tanaka, S., 1988, "HVEM and HREM of Interfaces in AlN Ceramics," *J. de Physique*, C5, pp. 189-194.
- Kim, K.S., Clifton, R.J. and Kumar, P., 1977, "A Combined Normal and Transverse Displacement Interferometer with an Application to Impact of Y-Cut Quartz," *J. Appl. Physics*, Vol. 48, pp. 4132-4139.
- Kim, Y.H., Chang, Y.S., Chou, N.J., and Kim, J., 1987, "Adhesion of Titanium Thin Films to Oxide Substrates," *J. Vac. Sci. Technol.*, A5(5), pp. 2890-2893.
- Kipp, M., and Grady, D., 1989, "Shock Compression and Release in High-Strength Ceramics," *Sandia Report*, SAND89-1461.
- Kumar, P. and Clifton, R.J., 1977a, "Optical Alignment of Impact faces for plate Impact Experiments," *J. Appl. Physics*, Vol. 48, pp. 1366-1367.
- Kumar, P. and Clifton, R.J., 1977b, "A Star-Shaped Flyer for Plate Impact Recovery Experiments," *J. Appl. Physics*, Vol. 48, p. 4850.
- Kumar, P. and Clifton, R.J., 1979, "Dislocation Motion and Generation in LiF Single Crystals Subjected to Plate-Impact," *J. Appl. Physics*, Vol. 50(7), pp. 4747-4762.
- Li, C.H. and Clifton, R.J., 1981, "Dynamic Stress-Strain Curves at Plastic Shear Strain Rates of  $10^5 \text{ s}^{-1}$ ," *AIP Conf. Proc., Shock Waves Condensed Matter*, Ed. Willis, W.J., pp 360-366.
- Mello, M.C., Prakash, V., and Clifton, R.J., 1991, "Multi-Point Interferometer for Monitoring Two Dimensional Wave Motion," to appear in *Proceedings of 1991 APS Topical Conference on Shock Compression of Condensed Matter*.
- Nagelberg, A. S., 1989, "The Effect of Processing Parameters on the Growth Rate and Microstructure of  $\text{Al}_2\text{O}_3$ /Metal Matrix Composites," *Mat. Res. Soc. Proc.*, Vol. 155, pp. 275-282.
- Raiser, G.F., Clifton, R.J. and Ortiz, M., 1990, "A Soft-Recovery Plate Impact Experiment for Studying Microcracking in Ceramics," *Mechanics of Materials*, Vol. 10, pp. 43.
- Rosenberg, Z. and Bless, S.J., 1986, "Determination of Dynamic Yield Strengths with Embedded



- Manganin Gages in Plate-Impact and Long-Rod Experiments," *Experimental Mechanics*, pp. 279-282.
- Rosenberg, Z., Brar, N.S. and Bless, S.J., 1991, "Dynamic High Pressure Properties of AlN Ceramic as Determined by Flyer Plate Impact," *Submitted for publication to J. Appl. Phys.*
  - Setchell, R.E., 1979, "Index of Refraction of Shock-Compressed Fuse Silica and Sapphire," *J. Appl. Physics*, Vol. 50(12), pp. 8186-8192.
  - Tong, W., 1991, "Pressure-Shear Impact Investigation of Strain-Rate History Effects in OFHC Copper," *Ph. D. Thesis, Brown University, Providence, RI.*
  - Tong, W., Clifton, R.J. and Huang, S., 1991, "Pressure-Shear Impact Investigation of Strain-Rate History Effects in OFHC Copper," *Submitted for Publication.*
  - Williams, R. and Keough, D.D., 1968, "Piezoresistive Response of Thin Films of Calcium and Lithium to Dynamic Loading," *Bull. Am. Phys. Soc.*, Series II, Vol. 12, p. 1127.
  - Wong, M.K.W., and Gupta, Y.M., 1991, "Dynamic Inclusion Analyses of Lateral Piezoresistance Gauges under Shock Wave Loading," *to appear in Proceedings of 1991 APS Topical Conference on Shock Compression of Condensed Matter.*
  - Zhou, M. and Clifton R.J., 1991, "Dynamic Ductile Rupture in a Spheroidized 1045 Steel," *in preparation.*